

Dissolved CO₂ stabilizes dissolution front and increases breakthrough porosity of natural porous materials

Y. Yang*¹, S. Bruns¹, S. L. S. Stipp¹ and H. O. Sørensen¹

¹ Nano-Science Center, Department of Chemistry, University of Copenhagen, Universitetsparken 5, DK-2100 Copenhagen, Denmark

* yyang@nano.ku.dk

ABSTRACT

When reactive fluids flow through a dissolving porous medium, conductive channels form, leading to fluid breakthrough. This phenomenon is important in geologic carbon storage, where the dissolution of CO₂ in water increases the acidity and produce microstructures significantly different from those in an intact reservoir. We demonstrate the controlling mechanism for the dissolution patterns in natural porous materials. This was done using numerical simulations based on high resolution digital models of North Sea chalk. We tested three model scenarios, and found that aqueous CO₂ dissolve porous media homogeneously, leading to large breakthrough porosity. In contrast, CO₂-free solution develops elongated convective channels in porous media, known as wormholes, and resulting in small breakthrough porosity. We further show that a homogeneous dissolution pattern appears because the sample size is smaller than the theoretical size of a developing wormhole. The result indicates that the presence of dissolved CO₂ expands the reactive subvolume of a porous medium, and thus enhances the geochemical alteration of reservoir structures and might undermine the sealing integrity of caprocks when minerals dissolve.

Introduction

A great challenge in predicting the consequences of geologic carbon storage (GCS) is to quantify the interaction between flowing reactive fluids and geologic formations.¹⁻⁸ This challenge requires considering a GCS reservoir as a constantly evolving confinement of fluids subject to geochemical and geomechanical instabilities.^{9, 10} Reactive infiltration instability (RII) is the morphological instability of a migrating dissolution front to heterogeneities in petrophysical properties. It controls the microstructural evolution of rock in an imposed flow field and is key to the self-organization of natural porous materials.¹¹⁻¹⁷ Identifying the trigger of this instability, as well as the chemical reactions important for the morphological development,^{18, 19} is especially useful for predicting the evolution of sealing integrity of caprocks and the geomechanical deformation of reservoir structures as host rocks are eroded away.

Morphological evolution of porous media caused by reactive infiltration instability can be described qualitative using dissolution patterns (homogeneous, ramified, channelized etc.,²⁰⁻²² see also Figure 1), or quantitatively using breakthrough porosity, φ_c , the macroscopic porosity of a sample when fluid breakthrough occurs.^{20, 23, 24} The strength of coupling between mineral dissolution rate and rock permeability is essential to this dynamic process and can be decomposed into 3 types of sensitivity.^{21, 25} The first is the sensitivity of flow field to rock microstructure determines how the reactants and products of water-rock interactions are conveyed in a flow field so the chemical reactions are kept away from equilibrium.²⁶⁻²⁹ This sensitivity can be affected by, among others, the geometry and texture of pore structures,³⁰⁻³⁴ the property and interactions between flowing fluids,³⁵⁻³⁸ as well as the body forces exerted by, e.g., gravitational or electrostatic fields.³⁹ The second sensitivity concerns the kinetic dependence of water-rock interactions to fluid composition, which determines the spatial variations of chemical

conversion (i.e., the extent of chemical reaction measured by the relative amount of reactant turned into product).⁴⁰ This sensitivity is often complicated by the intrinsic mineral heterogeneity in natural porous media⁴¹⁻⁴⁴ and by the large number of aqueous species involved in the reactions.^{45, 46} Lastly, the sensitivity of the rock microstructure to chemical conversion closes the loop of the positive feedback leading to RII.⁴⁷ This sensitivity reflects the density, molar weight and the solubility of the dissolving or precipitating minerals. If any of the three sensitivities becomes zero, the infiltration instability vanishes and the self-organization of a porous structure ceases.^{13, 48, 49}

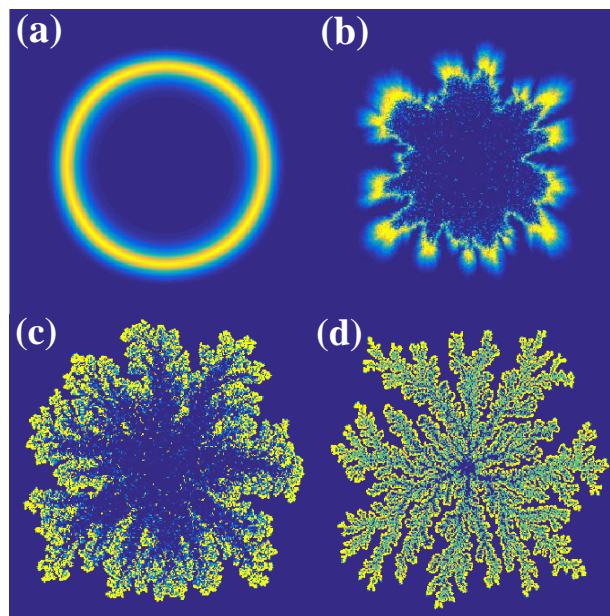


Figure 1. A qualitative demonstration of the dissolution front instability. The instability determines the morphology of dissolving porous media. (a) Stable dissolution front: mineral dissolution always takes place at the same distance from the injection point. (b) – (d): increasingly unstable dissolution fronts. The distance between dissolution front and the injection well can vary considerably. Yellow indicates the dissolving regions during the injection of a reactive fluid from the center of the 2D domain. The same amount of reactive fluid is being injected, and snapshots are taken after the same injection time. The instability caused the

changes, and a greater instability leads to a higher likelihood of material breakthrough with solid channelisation (wormholing).

Introducing CO₂ into a natural porous formation changes many variables mentioned above and thus affects all three types of sensitivity. For example, buoyant gaseous or supercritical CO₂ might induce Rayleigh-Taylor instability,⁵⁰ influencing the spreading of the reactive aqueous phase and the mixing between fluids.⁵¹ Dissolution of CO₂ in water changes many aspects of the kinetics of water-rock interactions. The mineral dissolution rates change because of a lowered pH and a stronger contribution from carbonic and bicarbonate species through surface complexation.^{52, 53} The apparent order of reaction, i.e., the sensitivity of reaction rate to reactant concentration, decreases because of the buffering effect of dissolved CO₂ as a weak acid.³² The apparent solubility of minerals can also be affected because of the changed ion activity and the buffered pH. The increased solubility is a thermodynamic driving force for the dissolution reactions. Meanwhile, it can also change the secondary mineral phases and as a result the sensitivity of solid architecture to the extent of reaction.^{7, 8, 54, 55} Moreover, the impact of CO₂ is related to the way gas is introduced into a geologic setting:^{56, 57} direct injection,⁵⁸ surface mixing⁵⁹ or wellbore mixing^{4, 60} all yield distinct pressure and solution compositions.

The dynamics of dissolving microstructures and, consequently, the CO₂ effect on the breakthrough properties of natural porous materials remain poorly understood for three reasons. First, structural heterogeneities (e.g., spatial variations in porosity and permeability) are perturbations for reaction front migration. These perturbations are amplified by infiltration instability. Thus, in a series of experiments, the initial microstructure must be the identical for meaningful comparison of results.^{19, 30, 31} Second, new models that preserve small scale heterogeneities in numerical simulations are essential.⁶¹⁻⁶³ The advancement of X-ray imaging

has allowed researchers to incorporate real microstructures of natural samples into numerical simulations.^{64, 65} However, such an operation usually requires binarisation (segmentation) of the image data. This is because of the limited applicability of governing equations derived from first principles (e.g., Navier-Stokes equations cannot be applied directly to a mixture of solid and fluids).^{66, 67} This “hard segmentation” reduces the information contained in each pixel and might erase the important heterogeneities that trigger the unstable migration of the dissolution front.^{68,}
⁶⁹ This caveat is especially significant when the imaging resolution is not sufficient to fully resolve the very fine grains and pores in materials such as chalk. A third reason is that simulating microstructural evolution is a free boundary problem of partial differential equations and often requires prohibitive computation even with binarised geometry.^{14, 48}

In this study we focus on the effect of dissolved CO₂ (as aqueous species) on the microstructural evolution of natural porous materials. The compositions of 3 reactive fluids, corresponding to different model scenarios, were used to flow through the simulation domain. We used high resolution X-ray tomography (25, 50 and 100 nm voxel size) to characterize the microstructures of natural samples from a North Sea chalk formation. Chalk is chosen as a fast dissolving model rock because it is the dominant bedrock in northwest Europe providing oil and gas reservoirs considered for GCS. After computing voxel specific porosities from the 32 bit images, the greyscale datasets were implemented directly into numerical simulations. The simulations allowed us to disentangle the effects of fluid composition from those of different initial microstructures. The simulated spatial and temporal evolutions of rock properties (porosity, permeability and surface area) helped outline the interplay between breakthrough porosity, wormholing and aqueous CO₂.

Methods and Materials

Three chalk samples from the Hod formation excavated from different locations of North Sea Basin were imaged with X-ray holotomography at 29.49 keV at ID22 of European Synchrotron Research Facility (ESRF).⁶¹ The 3D microstructure were reconstructed from 1999 radiographs at 25, 50 and 100 nm voxel resolutions and processed as described in detail in Bruns et al. Post reconstruction image processing included ring artefact removal according to Jha et al.,⁷⁰ followed by iterative nonlocal means denoising⁶⁶ and sharpening using the image deconvolution of Wang et al.⁷¹ Greyscale intensities of the voxels were then converted to localized porosity values using linear interpolation between the void phase and the carbonate phase as identified by a fit of a Gaussian mixture model.⁶⁷ The obtained greyscale data were imported into numerical simulations based on a previously developed reactor network model.²⁵ The model describes each imported voxel as a combination of 7 ideal reactors. The volume, permeability and specific surface area of each reactor were assigned according to the voxel size and porosity of neighboring voxels. Each simulation domain consisted of 100^3 32-bit voxels, corresponding to $15.625 \mu\text{m}^3$, $125.0 \mu\text{m}^3$ and $1000.0 \mu\text{m}^3$ for the three resolutions. A constant fluid velocity (50 $\mu\text{m/s}$) was imposed at the fluid inlet and outlet. Speciation calculations for the three model scenarios (ambient, premixing and direct injection, see Table 1) were conducted using PHREEQC (Version 3) with the *llnl* database.^{72, 73} The composition of seawater in scenario II was based on Nordstrom et al.⁷⁴ The Peng-Robinson equation of state was used to calculate fugacity coefficients.⁷⁵ The B-dot equation was used to calculate the activity coefficients of aqueous species in scenarios II and III.⁷⁶ We chose to use the rate law for calcite dissolution from Pokrovsky^{52, 53} to approximate the dissolution kinetics of chalk. The surface speciation is calculated based on the aqueous speciation in a closed free-drifting compartment where the

aqueous Ca concentration is used as the master variable that determines both the pH and the saturation index of calcite. The rates are then computed and compiled in Figure S1.

Table 1. The model scenarios.⁷⁴

Scenario	ChemID	Temperature (°C)	P_{CO2} (Bar)	Background Electrolytes	Initial pH*
I	01	25	1	n.a.	3.91
I	02	25	0	n.a.	3.91
II	03	25	25	Seawater**	3.65
II	04	25	0	Seawater**	3.65
III	05	100	250	1.0 M NaCl	3.09
III	06	100	0	1.0 M NaCl	3.09

* Adjusted by hydrochloric acid in the absence of CO₂

** Nordstrom and others (1979)

Results and Discussion

We use the rate of entropy production from fluid friction over the entire sample, S_p ($\text{nJ K}^{-1} \text{s}^{-1}$), to identify a breakthrough event. S_p quantifies the pressure drop in 3D and is calculated as

$$S_p = - \iiint_V (\mathbf{Q} \cdot \nabla P) dV / T \quad (1)$$

where V indicates an integration over the entire sample, \mathbf{Q} represents the volumetric flow rate ($\text{m}^3 \text{s}^{-1}$), P , the pressure (Pa) and T , the temperature (K). When porous media are eroded by reactive fluids, the evolution of S_p depends on the initial microstructure, the kinetics of the dissolution reaction(s) and the flow rate. Figure 2 shows two patterns of S_p evolution: the wormholing pattern, where solid channelisation can be identified, and the homogeneous pattern, where the whole domain dissolves evenly. During wormhole growth, S_p demonstrates one or more rapid drops, signifying the “necking” of regions with high porosities, *i.e.*, small breakthrough of fluid. Necking events are represented by local minima of S_p' , the first derivative of S_p with respect to time, and can thus be identified by inflection points (Figure 2a). Because of the structural heterogeneity of natural porous media, the critical porosity at which necking occurs, as well as the number of its occurrences, differs for each sample even with the same solution composition. In this study, we report the porosity at the global minimum of S_p' as the breakthrough porosity (φ_c , green arrowed in 2a). This choice does not imply the uniqueness of the necking event during percolation. Figure 2d shows cross sections of a wormholing sample before and after breakthrough and the corresponding spatial patterns of entropy generation. Formation of flow paths with higher permeability lead to the bypassing of fluid from the less porous regions. After breakthrough, a significant pressure drop occurs only at the neck of pores (e.g., $\varphi_a = 0.50$).

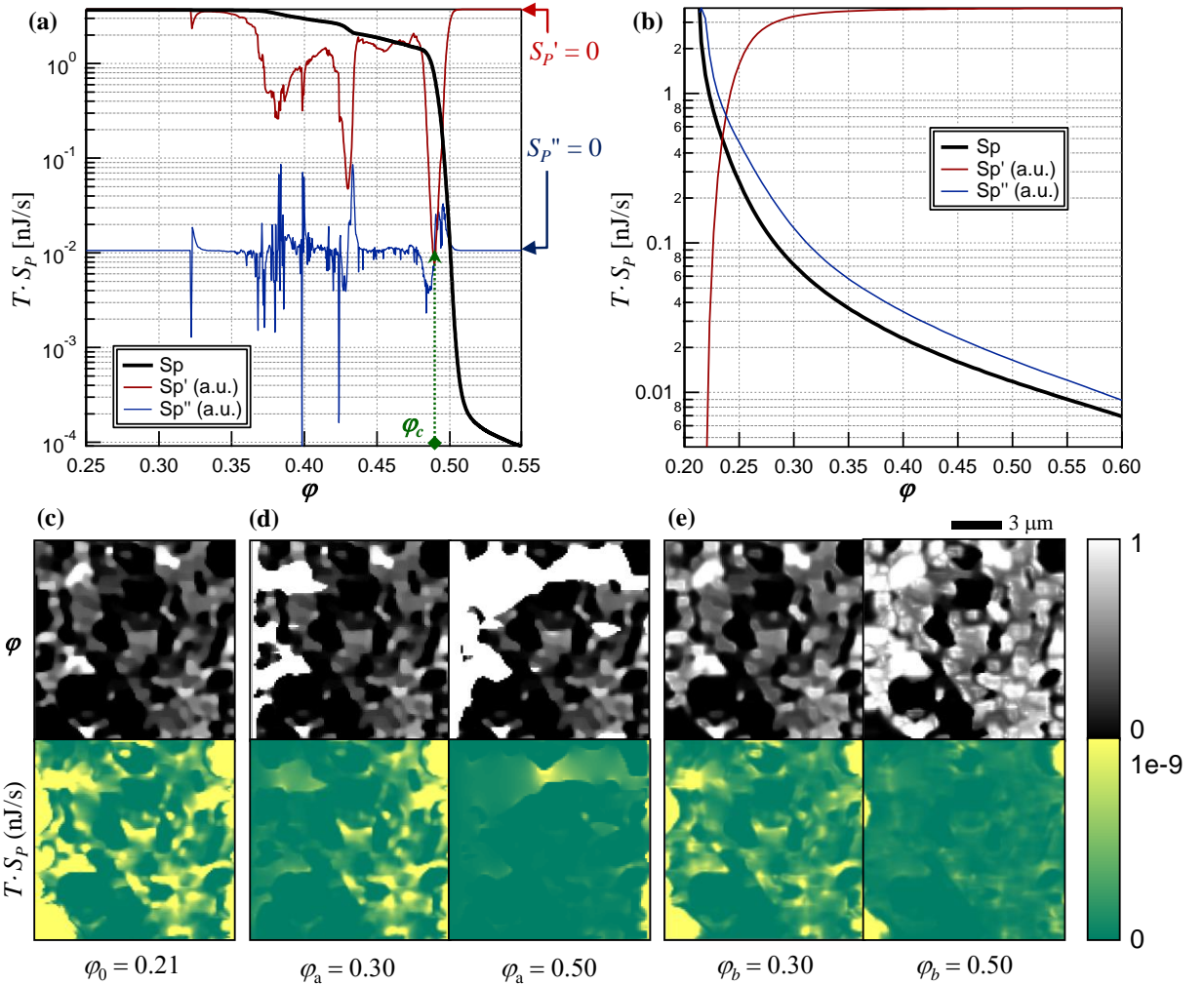


Figure 2. Typical temporal and spatial patterns of entropy generation (S_p) from fluid friction in developing porous structures. Evolution of S_p in isothermal (a) wormholing and (b) homogeneously dissolving systems. S_p' and S_p'' are first and second derivatives of S_p with respect to percolation time. We use the inflection point at the global minimum of S_p' to signify the occurrence of breakthrough (e.g., ϕ_c in a). When ϕ_c is greater than 1, no inflection exists and the medium dissolves homogeneously. (c) – (e) Cross sections of porosity (ϕ) and entropy production rate ($T \cdot S_p$) from 3D simulations based on GeoID 1832 (Table S1). Fluid flows from left to right. (c) The initial geometry. (d) A wormholing system before ($\phi_a = 0.30$) and after ($\phi_a = 0.50$) breakthrough. (e) A homogeneous dissolution system at the same reaction progresses ($\phi_b = 0.30$ and $\phi_b = 0.50$).

Figure 2b shows a temporal pattern of S_p where no abrupt pressure drop can be observed before the depletion of solid material. This pattern indicates a homogeneous dissolution where S_p increases monotonically. The spatial patterns in Figure 2e reveal that the morphology change does not show strong dependence on the flow direction, i.e. the entire sample behaves as a homogeneous medium despite its geometric complexity, and in different regions porosities decrease at similar rates. Because of the absence of a favored flow path, no significant fluid focusing occurs.

For each of the 40 samples (15 samples each from the 25 nm/pixel and 100 nm/pixel tomogram and 10 samples for the 50 nm/pixel tomogram) we developed 3 model scenarios and simulated the microstructural evolution with and without dissolved CO_2 , leading to 6 conditions (Table 1) and 240 instances of simulation (Table S1). Scenario I represents the ambient conditions where MilliQ water, equilibrated with 1 bar CO_2 , is percolating through the porous material at room temperature. In scenario II concentrated CO_2 is premixed with seawater at ambient temperature before injected into a geologic formation at intermediate partial pressure of CO_2 . This operation has been used in, e.g., the CarbFix project in Hellisheidi, Iceland.⁶⁰ Scenario III investigates a direct injection of CO_2 into deep formations where the supercritical CO_2 mixes with brine under reservoir conditions and then migrate away from the injecting well. The results are compared with percolations free of CO_2 . Hydrochloric acid is added in the absence of CO_2 so that solution pairs in each scenario have the same initial pH and therefore a initially comparable calcite dissolution rate. In addition to the breakthrough porosity, we also report the number of pore volumes until breakthrough (# of PV, i.e., the total volume of percolated fluid divided by the initial pore volume of a sample) whenever an S_p inflection can be identified. If a sample

dissolves homogeneously, the breakthrough porosity is reported as the difference between its initial porosity and 1. No # of PV is reported for these cases.

Figure 3 shows results of 240 simulations. In 74.2% of all the simulated percolations, dissolved CO₂ led to greater breakthrough porosity. This percentage exhibits scenario dependence, being 82.5% for the ambient scenario (I), 77.5% for the premixing scenario (II) and 62.5% for the direct inject scenario (III). In addition, all systems with CO₂ need less fluid to breakthrough than the CO₂ free systems. The differences are between one to two orders of magnitude. The results also show a weak initial porosity (φ_0) dependence. The “homogeneous boundaries” (dashed lines) decrease linearly with φ_0 because they reflect only the total amount of solid initially present and are results of mass balancing. Thus, a completely homogeneous dissolution does not reflect the initial geometric complexity. Also, the number of pore volumes (# of PV) decreases with increasing initial porosity because less fluid needed to breakthrough a more porous material. No significant resolution dependence of the results is observed.

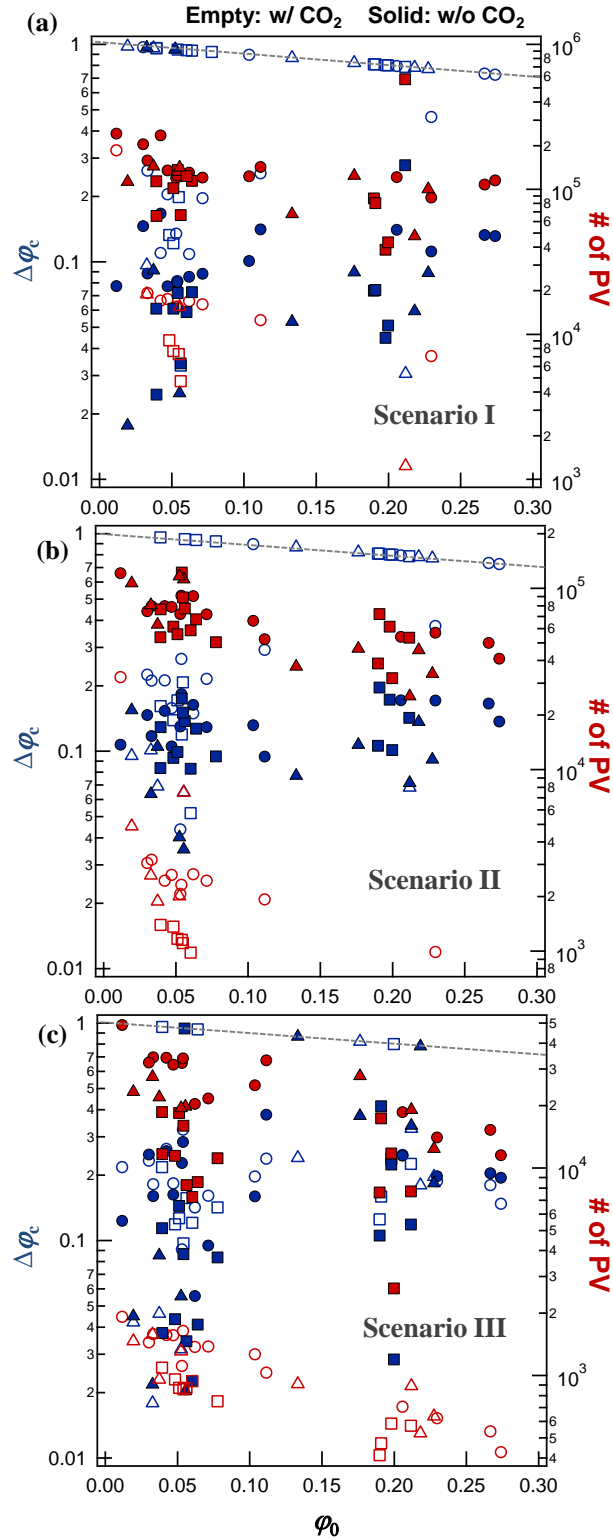


Figure 3. Breakthrough porosity and the corresponding number of pore volumes of fluid (# of PV, red symbols). $\Delta\phi_c$ (blue symbols) represents the difference between the breakthrough porosity (ϕ_c) and the initial porosity (ϕ_0) of a sample. All samples are cubic and consist of 1

million voxels. The empty symbols show results with CO₂ and the solid ones show systems free of CO₂. The shape of the symbols represents the voxel size: square – 100 nm, triangle – 50 nm and circle – 25 nm. The gray dashed line near the top of each figure draws the “homogeneous boundary” – corresponding to cases in which no inflection of S_p can be found before solid depletion (*i.e.*, the sample dissolves homogeneously throughout the percolation). For points on this boundary, the number of PV are not shown because of the difficulty in defining “breakthrough”. (a) Ambient conditions (Scenario I). (b) Premixing conditions (Scenario II). (c) Direct injection conditions (Scenario III).

Both the differences in the breakthrough porosity ($\Delta\phi_c$) and the number of pore volumes (# of PV) can be explained by the observed dissolution patterns. Given the same initial structure, the dissolution pattern is determined by distribution of reactants in the medium. Figure 4 shows the decrease of fluid reactivity (measured by reaction rate and pH) as a function of cumulative surface (CS), $\int_0^{\tau_{res}} SSA \cdot dt$, in the 3 model scenarios. The τ_{res} represents the residence time of fluid in the porous medium (s), and SSA, the specific surface area (m⁻¹). The physical significance of CS is the overall surface area the fluid “sees” as it travels through a medium. The curves therefore represent the chemical history of an isolated “fluid parcel”, an imaginary constituent of the flowing fluid, travelling along a streamline. Here we assume that the parcel only interacts with the solid on the streamline and does not exchange mass with other fluid parcels. As solid dissolves, the pH and the saturation index (SI) in the fluid parcel increase. Both effects slow down the reaction. The reaction front of the streamline is the position at which the reactivity of the fluid parcel drops to a very small value (e.g., 10⁻⁶ mol/m²/s in Figure 4). This definition suggests the equivalence of residence time and surface area in determining the reaction front. Although specific surface area (SSA) depends exclusively on the sample microstructure, the residence time (τ_{res}) relies on both the microstructure and the fluid flow rate. Consequently, different dissolution patterns can coexist in a system. This is because the patterns reflect the

competition between the reaction front and the cumulative surface within a region of interest (ROI). Given the same solution chemistry, one observes a homogeneous dissolution pattern when the fluid leaves the ROI without depleting reactivity. This is typical for fluids with a high apparent mineral solubility. The reaction front of these fluids appears only when residence time is sufficiently long or the specific surface area is large. If, in contrast, the reaction front is reached well before the fluid leaves the ROI, wormholes appear. The residence time can be increased by using a lower flow rate or a bigger sample (i.e., a large ROI). For example, in Figure S2 we show that with an ROI 5 times longer in the flow direction, changing flow rates alone can change the observed dissolution pattern.

Given sample size (i.e., ROI) and flow rate, the CS is fixed, and distinct dissolution patterns are most likely to occur when the ROI contain only one of the two reaction fronts. This is demonstrated by the shaded areas in Figure 4. These areas are left-bounded by the dissolution front of systems without CO₂ and right-bounded by those with dissolved CO₂. If the CS of a sample falls to the left of the shaded areas, the sample dissolves homogeneously. In contrast, if the CS falls to the right of the shaded areas, wormhole appears regardless of whether CO₂ is present. The fluid velocity in this study (50 μm/s) produced distributions of CS that overlap with these shaded areas. Therefore, the widths of the shaded regimes explain the percentages of different patterns observed in the model scenarios. In the ambient scenario (I) the reaction fronts with and without CO₂ are farthest from each other (the shaded area is widest in Figure 4a). Without CO₂, the ROI is bigger than the reactive volume and the wormholing pattern appears. With dissolved CO₂, the opposite is true. As a result 33 of the 40 comparisons (82.5%) show greater breakthrough porosity for systems with CO₂. In contrast, the two reaction fronts are very close to each other in the direct injection scenario (III, Figure 4c). Only 62.5% of the simulated

cases (25/40) showed that dissolved CO₂ increased the breakthrough porosity. The distance between the two reaction fronts is intermediate in the premixing scenario (Figure 4b), and so is the percentage (77.5%).

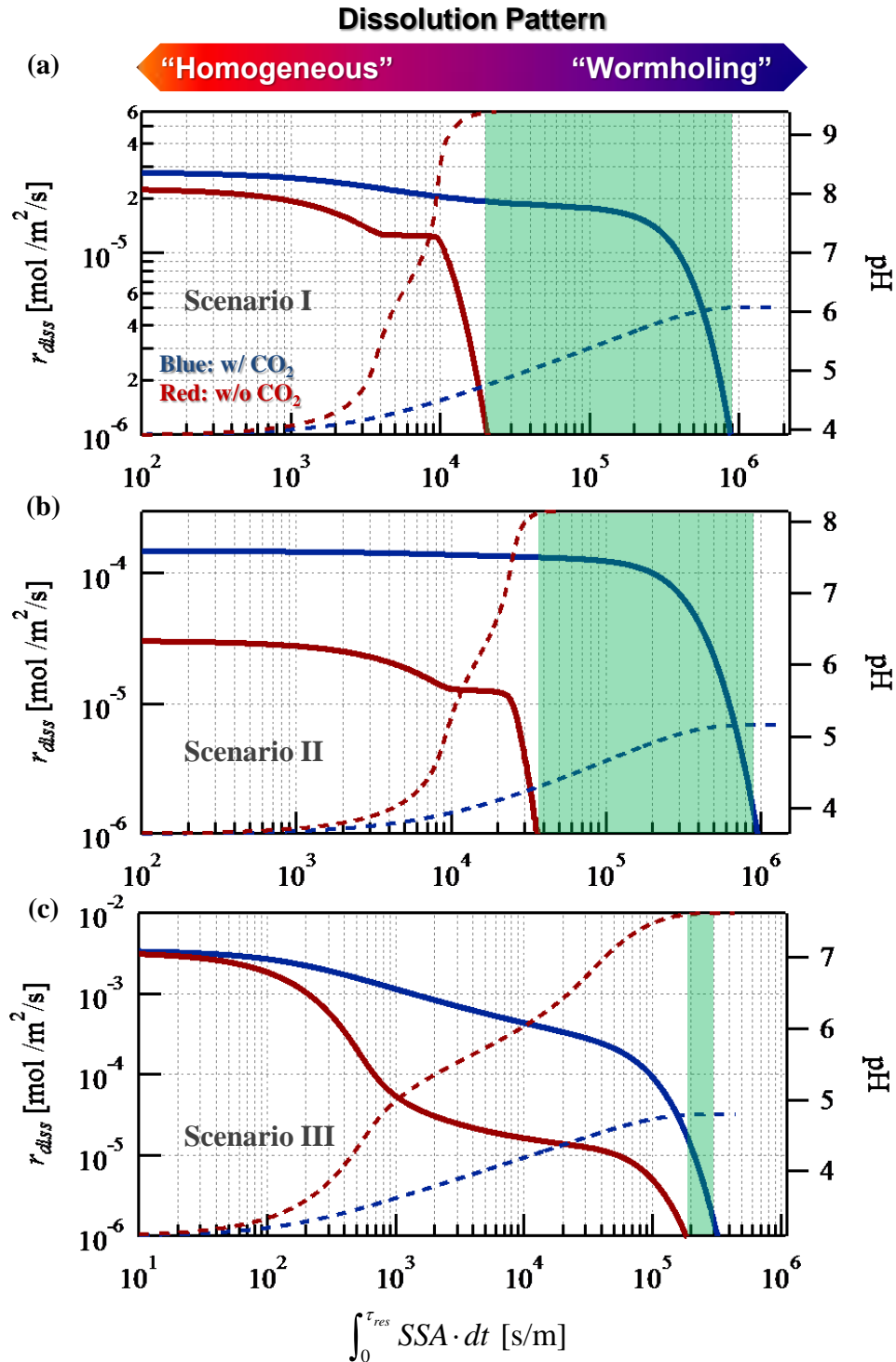


Figure 4. Decrease of calcite dissolution rate (solid lines) with cumulative surface area ($\int_0^{\tau_{res}} SSA \cdot dt$) in a free drifting system. The integral represents the overall surface area an isolated “parcel” of reactive fluid experiences before leaving the sample. A greater cumulative surface is more likely to generate wormholing patterns (and vice versa). Shaded regimes are

bounded by the dissolution fronts of the two chemical systems. Hence, percolations with and without CO₂ in these regimes often produce distinct dissolution patterns. Also shown are the evolutions of pH values (dashed lines). (a) Ambient conditions (Scenario I). (b) Premixing conditions (Scenario II). (c) Direct injection conditions (Scenario III).

Fluid focusing is an important reason why a wormholing pattern relates to lower breakthrough porosity because. Similarly, more effective use of geometric surface for reaction explains why systems with dissolved CO₂ need less fluid to breakthrough. Both phenomena are demonstrated in Figure 5, where a case study of microstructural evolution in scenario I is presented. The initial geometry for both simulations is given in Figure S3. The two systems start with the same percolative entropy production rate owing to identical initial geometry. The isothermal S_p for the system with CO₂ decreases gradually, indicating a homogeneous dissolution pattern. In contrast, the system without CO₂ showed sharp decrease in S_p near $\phi = 0.4$, suggesting significant necking of pores typical in wormhole growth. S_p without CO₂ drops below the one with CO₂ after an overall porosity of 0.45, suggesting the bypassing of flow through a fully developed wormhole. The pressure drop after this point is determined by the shape of the channel rather than the porosity of the sample. This redistribution of flow is fluid focusing and is a typical in wormhole growth. Also shown in Figure 5a is the evolution of reactive surface area (RSA). Although the two systems start with exactly the same geometric surface area, their RSA differ by almost one order of magnitude because of the rapid depletion of fluid reactivity in the CO₂-free system. The initial increase in RSA is characteristic to a system with infiltration instability. The decrease of RSA is caused by the depletion of solid material. Although RSA in both cases evolve with similar trends, their absolute difference increase with time, contributing to the difference in # of PV at breakthrough.

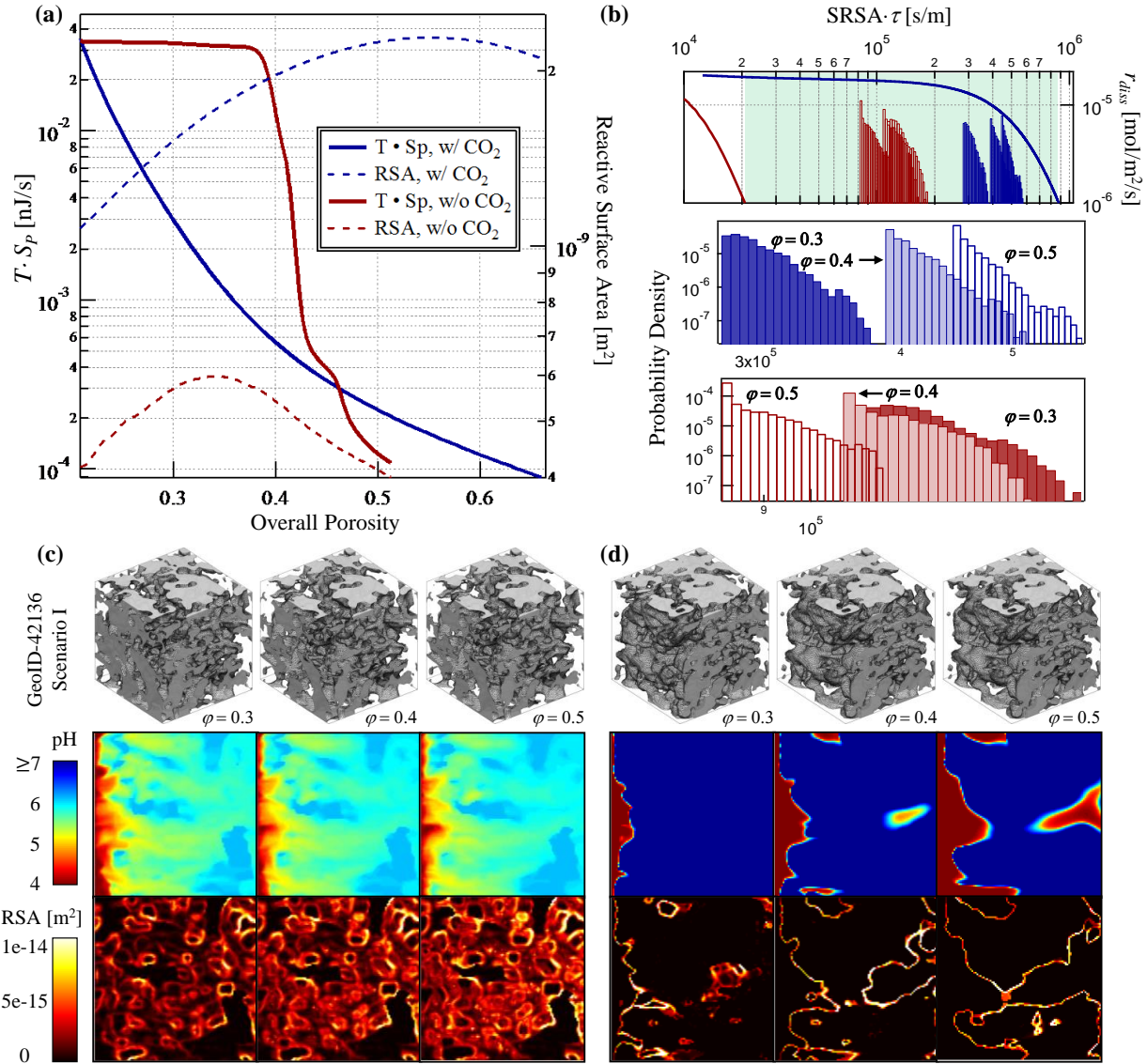


Figure 5. A case study of CO₂ effect on microstructural evolution (simulations uid-3813 vs. uid-96443). (a) Evolution of isothermal entropy generation rate ($T \cdot S_p$) and reactive surface area (RSA) with overall porosity as an indicator of reaction progress. (b) Distribution of residence time multiplied by specific reactive surface area (SRSA) in the context of calcite dissolution rates in Scenario I. The same shaded regime in Figure 4a is shown. The blue bars show the density function of fluid with CO₂ and the red bars, without. Also shown are microstructures, cross sections ($10 \times 10 \mu\text{m}^2$) of pH and of reactive surface distribution for percolations (c) with and (d) without CO₂.

Figures 5b to 5d compare the evolution of microstructures in the presence and absence of CO₂. In 5b the CS of the complete flow field is approximated by the product of specific reactive surface area (SRSA, m²/m³) and residence time distribution (RTD, giving the probability density of fluid parcels with residence time τ). The same shaded regime in Figure 4a is shown. Both distributions fall entirely into the regime between the two reaction fronts. As a result, the dissolution front with CO₂ cannot be observed in the simulation domain because it is beyond the sample size (blue bars). Meanwhile, the dissolution front without CO₂ is fully contained in the domain. This is because the sample provides approximately 10 times more cumulative surface required to reach the front (the maximum distance from the injection point to where the dissolution rate drops to zero, the red bars). The development of the distributions at different overall porosities ($\phi = 0.3, 0.4$ and 0.5) can be decomposed into two parts. The morphing of their shapes reflects the redistribution of fluid as the micropore evolves. The lower bound of the distribution represents the flow pathways with minimum flow resistance. As the sample dissolves, the mean residence time shifts leftwards indicating that the tendency of fluid to focus on the more permeable pathways. Fluid focusing during wormholing is directly reflected in the standard deviations. With CO₂ the standard deviation of the cumulative surface increases from 14769.9 s/m for $\phi = 0.3$ to 16137.8 s/m for $\phi = 0.5$, suggesting more uniform fluid distribution. In contrast, without CO₂ the number decreased from 10071.5 s/m to 6464.07 s/m at the same overall porosities. Therefore, much less geometric surface is in contact with reactive solution during wormhole growth (*e.g.*, spatial distribution of RSA in figures 5c and d). The development of reactive surface determines the horizontal shifting of the distributions. With dissolved CO₂, the maximum of RSA appears after an overall porosity of 0.5, and thus increasing the mean of the distribution. In contrast, the overall RSA free of CO₂ decreases after an overall porosity of

0.35, shifting the entire distribution of cumulative surface leftward. The spatial distribution of pH shows that the buffering effect of dissolved CO₂ increases the apparent solubility of calcite in the fluid and thus the local dissolution rate. Together with greater RSA, the presence of CO₂ results in much faster breakthrough (significantly lowered # of PV in all cases) although it increases the breakthrough porosity in 74.2% of the cases.

The CO₂ effect on breakthrough porosity has a few implications. Mineral dissolution serves as a trigger for many water-rock interactions. In GCS, dissolution reactions provide cations for carbon mineralization while initiate microstructural evolution that determines the mechanical strength of a formation. Also, changing the solid matrix can the potentially mobilize contaminants. A greater instability of the dissolution front, often associated with wormholing, is favored when geomechanical stability is desirable. This is because lower breakthrough porosity leads to a structure that dissipates injected fluid effectively without removing much solid materials serving as mechanical support. Meanwhile, a wide spread of fluid reactivity often observed in homogeneous dissolution increases the likelihood of contaminant mobilization. Our results show that dissolved CO₂ stabilizes the migration of dissolution front by increasing the cumulative surface required for breakthrough, making wormholing less likely within a given sample size. CO₂ also shortens dramatically the time for breakthrough. These complications, in addition to brine acidification, may constitute further challenges to engineering GCS.

ASSOCIATED CONTENT

Supporting Information. Calcite dissolution rate based on 3 rate laws available in the literature, for the 3 model scenarios. Cross sections of simulations showing the coexistence of different dissolution patterns within one sample at various flow rates. The initial geometry on which the case study presented in Figure 5 is based. Tabulated results of all simulations.

AUTHOR INFORMATION

Corresponding Author

* yiyang@nano.ku.dk

Author Contributions

YY designed the research and conducted the simulations. SB processed the tomography data. HOS and SLSS supervised the research.

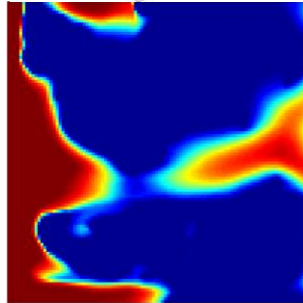
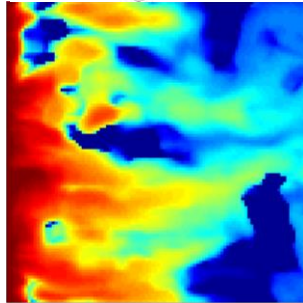
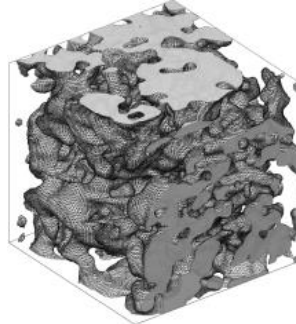
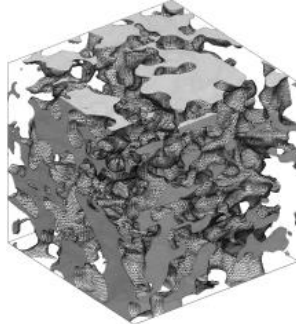
ACKNOWLEDGMENTS

We thank Heikki Suhonen at the ID22 beamline at ESRF (The European Synchrotron) for technical support. We are grateful to F. Engstrøm from Maersk Oil and Gas A/S for providing the sample. YY deeply appreciates Dr. K. Dideriksen for reviewing the manuscript and for the thought provoking discussions. Funding for this project was provided by the Innovation Fund Denmark, through the CINEMA project, the Innovation Fund Denmark and Maersk Oil and Gas A/S, through the P³ project as well as the European Commission, Horizon 2020 Research and Innovation Programme under the Marie Skłodowska-Curie Grant Agreement No 653241. We thank the Danish Council for Independent Research for support for synchrotron beamtime through DANSCATT.

TOC

With CO₂

Without CO₂



REFERENCES

1. Bourg, I. C.; Beckingham, L. E.; DePaolo, D. J., The Nanoscale Basis of CO₂ Trapping for Geologic Storage. *Environmental science & technology* **2015**, *49*, (17), 10265-10284.
2. DePaolo, D. J.; Cole, D. R., Geochemistry of Geologic Carbon Sequestration: An Overview. *Reviews in Mineralogy and Geochemistry* **2013**, *77*, (1), 1-14.
3. Alfredsson, H. A.; Oelkers, E. H.; Hardarsson, B. S.; Franzson, H.; Gunnlaugsson, E.; Gislason, S. R., The geology and water chemistry of the Hellisheidi, SW-Iceland carbon storage site. *International Journal of Greenhouse Gas Control* **2013**, *12*, 399-418.
4. Gislason, S. R.; Wolff-Boenisch, D.; Stefansson, A.; Oelkers, E. H.; Gunnlaugsson, E.; Sigurdardottir, H.; Sigfusson, B.; Broecker, W. S.; Matter, J. M.; Stute, M.; Axelsson, G.; Fridriksson, T., Mineral sequestration of carbon dioxide in basalt: A pre-injection overview of the CarbFix project. *International Journal of Greenhouse Gas Control* **2010**, *4*, (3), 537-545.
5. Bentham, M.; Kirby, M., CO₂ storage in saline aquifers. *Oil & gas science and technology* **2005**, *60*, (3), 559-567.
6. Ellis, B. R.; Peters, C. A., 3D Mapping of calcite and a demonstration of its relevance to permeability evolution in reactive fractures. *Advances in Water Resources* **2015**.
7. Ellis, B. R.; Fitts, J. P.; Bromhal, G. S.; McIntyre, D. L.; Tappero, R.; Peters, C. A., Dissolution-driven permeability reduction of a fractured carbonate caprock. *Environmental engineering science* **2013**, *30*, (4), 187-193.
8. Deng, H.; Ellis, B. R.; Peters, C. A.; Fitts, J. P.; Crandall, D.; Bromhal, G. S., Modifications of Carbonate Fracture Hydrodynamic Properties by CO₂-Acidified Brine Flow. *Energy & Fuels* **2013**, *27*, (8), 4221-4231.
9. Emmanuel, S.; Anovitz, L. M.; Day-Stirrat, R. J., Effects of Coupled Chemo-Mechanical Processes on the Evolution of Pore-Size Distributions in Geological Media. *Reviews in Mineralogy and Geochemistry* **2015**, *80*, (1), 45-60.
10. Hubbert, M. K.; Willis, D. G., Mechanics of hydraulic fracturing. **1972**.
11. Szymczak, P.; Ladd, A. J., Reactive-infiltration instabilities in rocks. Part 2. Dissolution of a porous matrix. *Journal of Fluid Mechanics* **2014**, *738*, 591-630.
12. Szymczak, P.; Ladd, A. J. C., Reactive-infiltration instabilities in rocks. Fracture dissolution. *Journal of Fluid Mechanics* **2012**, *702*, 239-264.
13. Ortoleva, P.; Chadam, J.; Merino, E.; Sen, A., Geochemical self-organization II: the reactive-infiltration instability. *Am. J. Sci* **1987**, *287*, 1008-1040.
14. Chadam, J.; Hoff, D.; Merino, E.; Ortoleva, P.; Sen, A., Reactive Infiltration Instabilities. *IMA Journal of Applied Mathematics* **1986**, *36*, (3), 207-221.
15. Steefel, C. I.; Lasaga, A. C., A coupled model for transport of multiple chemical-species and kinetic precipitation dissolution reactions with application to reactive flow in single-phase hydrothermal systems. *American Journal of science* **1994**, (294), 529-592.
16. Steefel, C. I.; Lasaga, A. C. In *Evolution of dissolution patterns: Permeability change due to coupled flow and reaction*, ACS symposium series, 1990; Oxford University Press: 1990; pp 212-225.
17. Hinch, E.; Bhatt, B., Stability of an acid front moving through porous rock. *Journal of Fluid Mechanics* **1990**, *212*, 279-288.

18. Hao, Y.; Smith, M.; Sholokhova, Y.; Carroll, S., CO₂-induced dissolution of low permeability carbonates. Part II: Numerical modeling of experiments. *Advances in Water Resources* **2013**, *62, Part C*, 388-408.
19. Cao, P.; Karpyn, Z. T.; Li, L., The role of host rock properties in determining potential CO₂ migration pathways. *International Journal of Greenhouse Gas Control* **2016**, *45*, 18-26.
20. Fredd, C. N.; Fogler, H. S., Influence of transport and reaction on wormhole formation in porous media. *AIChE Journal* **1998**, *44*, (9), 1933-1949.
21. Golfier, F.; Zarcone, C.; Bazin, B.; Lenormand, R.; Lasseux, D.; Quintard, M., On the ability of a Darcy-scale model to capture wormhole formation during the dissolution of a porous medium. *Journal of Fluid Mechanics* **2002**, *457*, 213-254.
22. Glasbergen, G.; Kalia, N.; Talbot, M. S. In *The Optimum Injection Rate for Wormhole Propagation: Myth or Reality?*, 8th European Formation Damage Conference, 2009; Society of Petroleum Engineers: 2009.
23. Fredd, C. N.; Scott Fogler, H., The kinetics of calcite dissolution in acetic acid solutions. *Chemical Engineering Science* **1998**, *53*, (22), 3863-3874.
24. Thompson, K. E.; Fogler, H. S., Modeling flow in disordered packed beds from pore-scale fluid mechanics. *AIChE Journal* **1997**, *43*, (6), 1377-1389.
25. Yang, Y.; Bruns, S.; Stipp, S. L. S.; Sørensen, H. O., Reactive infiltration instability amplifies the difference between geometric and reactive surface areas in natural porous materials (under review). **2016**.
26. Brunet, J.-P. L.; Li, L.; Karpyn, Z. T.; Kutchko, B. G.; Strazisar, B.; Bromhal, G., Dynamic Evolution of Cement Composition and Transport Properties under Conditions Relevant to Geological Carbon Sequestration. *Energy & Fuels* **2013**, *27*, (8), 4208-4220.
27. Gale, J.; Hendriks, C.; Turkenberg, W.; Huerta, N. J.; Bryant, S. L.; Strazisar, B. R.; Hesse, M., 10th International Conference on Greenhouse Gas Control Technologies Dynamic alteration along a fractured cement/cement interface: Implications for long term leakage risk along a well with an annulus defect. *Energy Procedia* **2011**, *4*, 5398-5405.
28. Huerta, N. J.; Hesse, M. A.; Bryant, S. L.; Strazisar, B. R.; Lopano, C. L., Experimental Evidence for Self-Limiting Reactive Flow through a Fractured Cement Core: Implications for Time-Dependent Wellbore Leakage. *Environmental Science & Technology* **2013**, *47*, (1), 269-275.
29. Zhang, L.; Dzombak, D. A.; Nakles, D. V.; Brunet, J.-P. L.; Li, L., Reactive Transport Modeling of Interactions between Acid Gas (CO₂ + H₂S) and Pozzolan-Amended Wellbore Cement under Geologic Carbon Sequestration Conditions. *Energy & Fuels* **2013**, *27*, (11), 6921-6937.
30. Menke, H. P.; Bijeljic, B.; Andrew, M. G.; Blunt, M. J., Dynamic Three-Dimensional Pore-Scale Imaging of Reaction in a Carbonate at Reservoir Conditions. *Environmental science & technology* **2015**, *49*, (7), 4407-4414.
31. Noiriël, C., Resolving Time-dependent Evolution of Pore-Scale Structure, Permeability and Reactivity using X-ray Microtomography. *Reviews in Mineralogy and Geochemistry* **2015**, *80*, (1), 247-285.

32. Noiriél, C.; Luquot, L.; Madé, B.; Raimbault, L.; Gouze, P.; van der Lee, J., Changes in reactive surface area during limestone dissolution: An experimental and modelling study. *Chemical Geology* **2009**, *265*, (1–2), 160-170.
33. Noiriél, C.; Madé, B.; Gouze, P., Impact of coating development on the hydraulic and transport properties in argillaceous limestone fracture. *Water Resources Research* **2007**, *43*, (9), n/a-n/a.
34. Noiriél, C.; Gouze, P.; Bernard, D., Investigation of porosity and permeability effects from microstructure changes during limestone dissolution. *Geophysical Research Letters* **2004**, *31*, (24), n/a-n/a.
35. Jha, B.; Juanes, R., Coupled multiphase flow and poromechanics: A computational model of pore pressure effects on fault slip and earthquake triggering. *Water Resources Research* **2014**, *50*, (5), 3776-3808.
36. Nicolaides, C.; Jha, B.; Cueto-Felgueroso, L.; Juanes, R., Impact of viscous fingering and permeability heterogeneity on fluid mixing in porous media. *Water Resources Research* **2015**, *51*, (4), 2634-2647.
37. Matin, R.; Misztal, M. K.; Hernandez-Garcia, A.; Mathiesen, J., Evaluation of the Finite Element Lattice Boltzmann Method for Binary Fluid Flows. *arXiv preprint arXiv:1608.01906* **2016**.
38. Misztal, M. K.; Matin, R.; Hernandez, A.; Mathiesen, J., Two-phase Flow Simulations Using the Lattice Boltzmann Method on Unstructured Grids. **2015**.
39. Carballido-Landeira, J.; Trevelyan, P. M. J.; Almarcha, C.; De Wit, A., Mixed-mode instability of a miscible interface due to coupling between Rayleigh-Taylor and double-diffusive convective modes. *Physics of Fluids* **2013**, *25*, (2), 024107.
40. Levenspiel, O., *Chemical reaction engineering*. Wiley & Sons, Inc.: 1999.
41. Yang, Y.; Min, Y.; Lococo, J.; Jun, Y.-S., Effects of Al/Si ordering on feldspar dissolution: Part I. Crystallographic control on the stoichiometry of dissolution reaction. *Geochimica et Cosmochimica Acta* **2014**, *126*, 574-594.
42. Yang, Y.; Min, Y.; Jun, Y.-S., Effects of Al/Si ordering on feldspar dissolution: Part II. The pH dependence of plagioclases' dissolution rates. *Geochimica et Cosmochimica Acta* **2014**, *126*, 595-613.
43. Gouze, P.; Luquot, L., X-ray microtomography characterization of porosity, permeability and reactive surface changes during dissolution. *Journal of Contaminant Hydrology* **2011**, *120–121*, 45-55.
44. Zachara, J.; Brantley, S.; Chorover, J.; Ewing, R.; Kerisit, S.; Liu, C.; Perfect, E.; Rother, G.; Stack, A. G., Internal Domains of Natural Porous Media Revealed: Critical Locations for Transport, Storage, and Chemical Reaction. *Environmental Science & Technology* **2016**, *50*, (6), 2811-2829.
45. Lu, J.; Kharaka, Y. K.; Thordsen, J. J.; Horita, J.; Karamalidis, A.; Griffith, C.; Hakala, J. A.; Ambats, G.; Cole, D. R.; Phelps, T. J., CO₂-rock-brine interactions in Lower Tuscaloosa Formation at Cranfield CO₂ sequestration site, Mississippi, USA. *Chemical Geology* **2012**, *291*, 269-277.
46. Zheng, L.; Apps, J. A.; Spycher, N.; Birkholzer, J. T.; Kharaka, Y. K.; Thordsen, J.; Beers, S. R.; Herkelrath, W. N.; Kakouros, E.; Trautz, R. C., Geochemical modeling of changes

- in shallow groundwater chemistry observed during the MSU-ZERT CO₂ injection experiment. *International Journal of Greenhouse Gas Control* **2012**, 7, 202-217.
47. Upadhyay, V. K.; Szymczak, P.; Ladd, A. J., Initial conditions or emergence: What determines dissolution patterns in rough fractures? *Journal of Geophysical Research: Solid Earth* **2015**, 120, (9), 6102-6121.
 48. Ortoleva, P. J., *Geochemical self-organization*. Oxford University Press: Clarendon Press: 1994.
 49. Ortoleva, P.; Merino, E.; Moore, C.; Chadam, J., Geochemical self-organization I: reaction-transport feedbacks and modeling approach. *Am. J. Sci* **1987**, 287, (10), 979-1007.
 50. Kalisch, H.; Mitrovic, D.; Nordbotten, J. M., Rayleigh–Taylor instability of immiscible fluids in porous media. *Continuum Mechanics and Thermodynamics* **2016**, 28, (3), 721-731.
 51. Thomas, C.; Loodts, V.; Rongy, L.; De Wit, A., Convective dissolution of CO₂ in reactive alkaline solutions: Active role of spectator ions. *International Journal of Greenhouse Gas Control* **2016**, 53, 230-242.
 52. Pokrovsky, O. S.; Golubev, S. V.; Schott, J.; Castillo, A., Calcite, dolomite and magnesite dissolution kinetics in aqueous solutions at acid to circumneutral pH, 25 to 150 C and 1 to 55 atm pCO₂: new constraints on CO₂ sequestration in sedimentary basins. *Chemical geology* **2009**, 265, (1), 20-32.
 53. Pokrovsky, O. S.; Golubev, S. V.; Schott, J., Dissolution kinetics of calcite, dolomite and magnesite at 25 C and 0 to 50 atm pCO₂. *Chemical Geology* **2005**, 217, (3), 239-255.
 54. Deng, H.; Fitts, J. P.; Crandall, D.; McIntyre, D.; Peters, C. A., Alterations of Fractures in Carbonate Rocks by CO₂-Acidified Brines. *Environmental Science & Technology* **2015**, 49, (16), 10226-10234.
 55. Fitts, J. P.; Peters, C. A., Caprock Fracture Dissolution and CO₂ Leakage. *Reviews in Mineralogy and Geochemistry* **2013**, 77, (1), 459-479.
 56. Shariatipour, S. M.; Mackay, E. J.; Pickup, G. E., An engineering solution for CO₂ injection in saline aquifers. *International Journal of Greenhouse Gas Control* **2016**, 53, 98-105.
 57. Emami-Meybodi, H.; Hassanzadeh, H.; Green, C. P.; Ennis-King, J., Convective dissolution of CO₂ in saline aquifers: Progress in modeling and experiments. *International Journal of Greenhouse Gas Control* **2015**, 40, 238-266.
 58. Kumar, A.; Noh, M. H.; Ozah, R. C.; Pope, G. A.; Bryant, S. L.; Sepehrnoori, K.; Lake, L. W., Reservoir Simulation of CO₂ Storage in Aquifers.
 59. Burton, M.; Bryant, S. L., Eliminating Buoyant Migration of Sequestered CO₂ Through Surface Dissolution: Implementation Costs and Technical Challenges.
 60. Matter, J. M.; Stute, M.; Snæbjörnsdóttir, S. Ó.; Oelkers, E. H.; Gislason, S. R.; Aradóttir, E. S.; Sigfusson, B.; Gunnarsson, I.; Sigurdardóttir, H.; Gunnlaugsson, E., Rapid carbon mineralization for permanent disposal of anthropogenic carbon dioxide emissions. *Science* **2016**, 352, (6291), 1312-1314.
 61. Muter, D.; Sorensen, H.; Jha, D.; Harti, R.; Dalby, K.; Suhonen, H.; Feidenhans'l, R.; Engstrom, F.; Stipp, S., Resolution dependence of petrophysical parameters derived from X-ray tomography of chalk. *Applied Physics Letters* **2014**, 105, (4).

62. Gooya, R.; Bruns, S.; Müter, D.; Moaddel, A.; Harti, R.; Stipp, S.; Sørensen, H., Effect of tomography resolution on the calculated microscopic properties of porous materials: Comparison of sandstone and carbonate rocks. *Applied Physics Letters* **2016**, *109*, (10), 104102.
63. Müter, D.; Pedersen, S.; Sørensen, H. O.; Feidenhans'l, R.; Stipp, S. L. S., Improved segmentation of X-ray tomography data from porous rocks using a dual filtering approach. *Computers & Geosciences* **2012**, *49*, 131-139.
64. Blunt, M. J.; Bijeljic, B.; Dong, H.; Gharbi, O.; Iglauer, S.; Mostaghimi, P.; Paluszny, A.; Pentland, C., Pore-scale imaging and modelling. *Advances in Water Resources* **2013**, *51*, 197-216.
65. Steefel, C. I.; Beckingham, L. E.; Landrot, G., Micro-Continuum Approaches for Modeling Pore-Scale Geochemical Processes. *Reviews in Mineralogy and Geochemistry* **2015**, *80*, (1), 217-246.
66. Molins, S., Reactive Interfaces in Direct Numerical Simulation of Pore-Scale Processes. *Reviews in Mineralogy and Geochemistry* **2015**, *80*, (1), 461-481.
67. Molins, S.; Trebotich, D.; Steefel, C. I.; Shen, C., An investigation of the effect of pore scale flow on average geochemical reaction rates using direct numerical simulation. *Water Resources Research* **2012**, *48*, (3).
68. Bruns, S.; Stipp, S. L. S.; Sørensen, H. O., Looking for the Signal: A Guide to Iterative Noise and Artefact Removal in X-ray Tomography Reconstructions of Reservoir Rocks. *Water Resources Research (under review)* **2016**.
69. Bruns, S.; Sørensen, H. O.; Stipp, S. L. S., Rock Properties of Compacted North Sea Chalks characterized by Greyscale Analysis. *Water Resources Research (under review)* **2016**.
70. Jha, D.; Sørensen, H. O.; Dobberschütz, S.; Feidenhans; apos; l, R.; Stipp, S. L. S., Adaptive center determination for effective suppression of ring artifacts in tomography images. *Applied Physics Letters* **2014**, *105*, (14), 143107.
71. Wang, Y.; Yang, J.; Yin, W.; Zhang, Y., A New Alternating Minimization Algorithm for Total Variation Image Reconstruction. *SIAM Journal on Imaging Sciences* **2008**, *1*, (3), 248-272.
72. Appelo, C. A. J.; Verweij, E.; Schäfer, H., A hydrogeochemical transport model for an oxidation experiment with pyrite/calcite/exchangers/organic matter containing sand. *Applied Geochemistry* **1998**, *13*, (2), 257-268.
73. Daveler, S. A.; Wolery, T. J., EQPT, A Data File Preprocessor for the EQ3/6 Software Package: User's Guide and Related Documentation (Version 7.0). *Lawrence Livermore National Laboratory, UCRL-MA-110662 PT II* **1992**, 1-89.
74. Nordstrom, D. K.; Plummer, L. N.; Wigley, T. M. L.; Wolery, T. J.; Ball, J. W.; Jenne, E. A.; Bassett, R. L.; Crerar, D. A.; Florence, T. M.; Fritz, B.; Hoffman, M.; Holdren, G. R.; Lafon, G. M.; Mattigod, S. V.; McDuff, R. E.; Morel, F.; Reddy, M. M.; Sposito, G.; Thraillkill, J., A Comparison of Computerized Chemical Models for Equilibrium Calculations in Aqueous Systems. In *Chemical Modeling in Aqueous Systems*, AMERICAN CHEMICAL SOCIETY: 1979; Vol. 93, pp 857-892.
75. Stryjek, R.; Vera, J., PRSV: An improved Peng—Robinson equation of state for pure compounds and mixtures. *The canadian journal of chemical engineering* **1986**, *64*, (2), 323-333.
76. Pitzer, K.; Brewer, L., revised edition of Thermodynamics by GN Lewis and M. Randall. In McGraw-Hill, New York, NY: 1961.

Supporting Information for

Dissolved CO₂ stabilizes dissolution front and
increases breakthrough porosity of natural porous
materials

Y. Yang, S. Bruns, S. L. S. Stipp and H. O. Sørensen*

Nano-Science Center, Department of Chemistry, University of Copenhagen

Universitetsparken 5, DK-2100 Copenhagen, Denmark

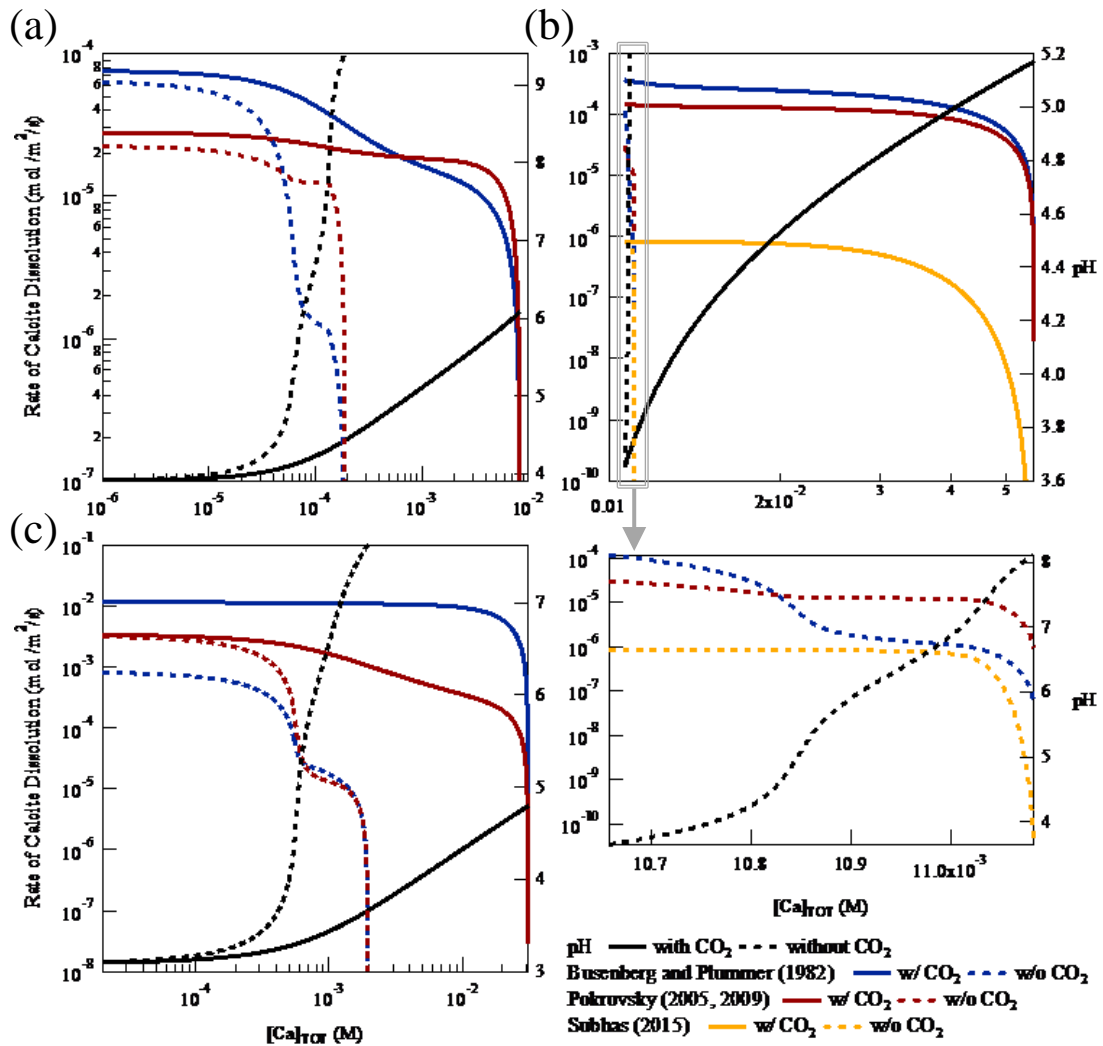


Figure S1. Rate of calcite dissolution in a closed (free-drifting) system based on Busenberg and Plummer,¹ Pokrovsky^{2,3} and Subhas⁴ in the model scenarios: (a) Ambient, (b) Premixing and (c) Direct injection.

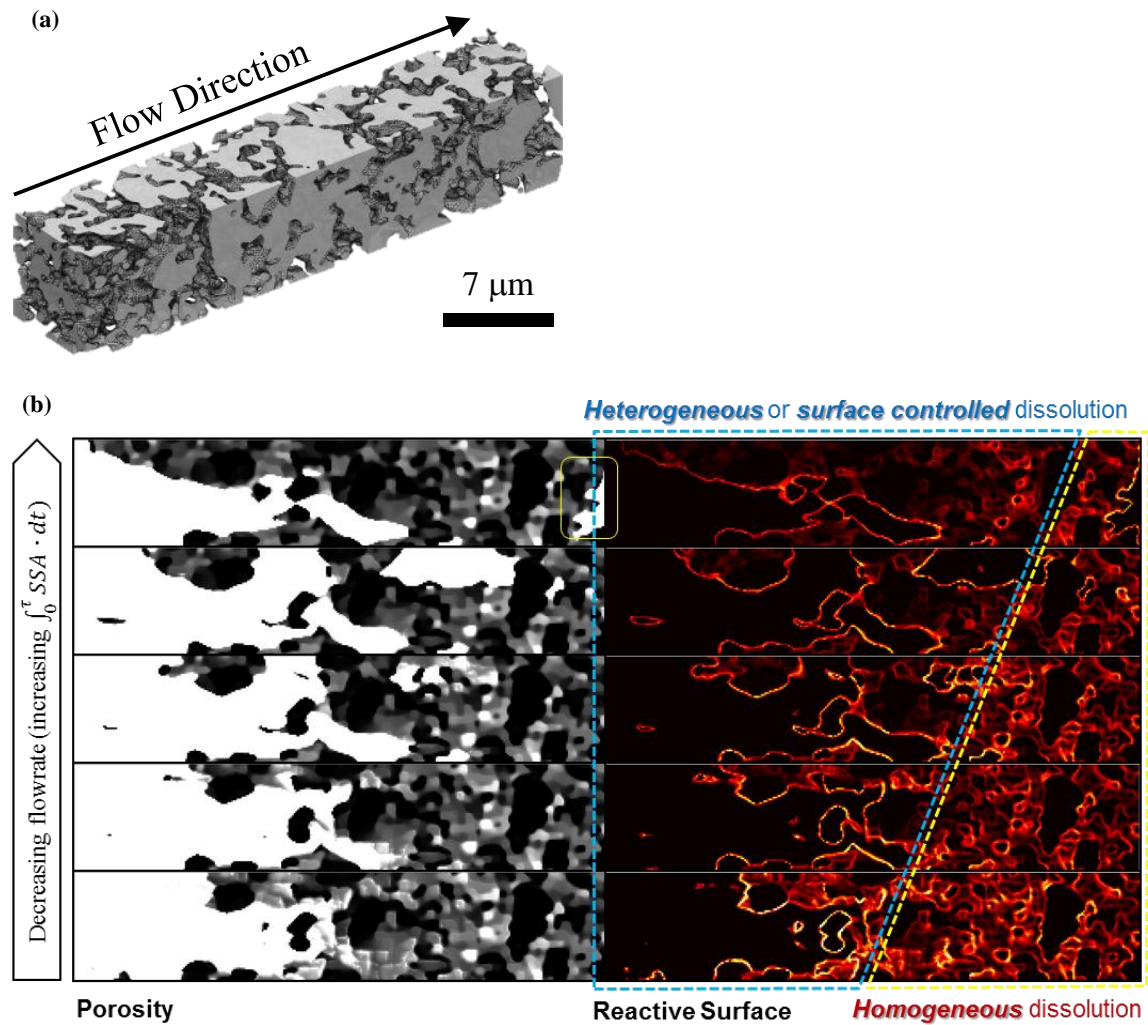


Figure S2. Simulations showing the coexistence of a homogeneously dissolving region and a heterogeneous or surface controlled (wormholing) region within a sample. The sample is longer in the flow direction than other samples so the cumulative surface is sufficiently large to contain the reaction front. Decreasing flowrate further increases the residence time and thus the cumulative surface. A first order rate law was used. (a) Simulation setup. The fluid flows from left to right. (b) Microstructures of the same sample at $\phi = 0.5$ with varying flowrates. Note that with the lowest flowrate (top row in b) the breakthrough has occurred (yellow box).

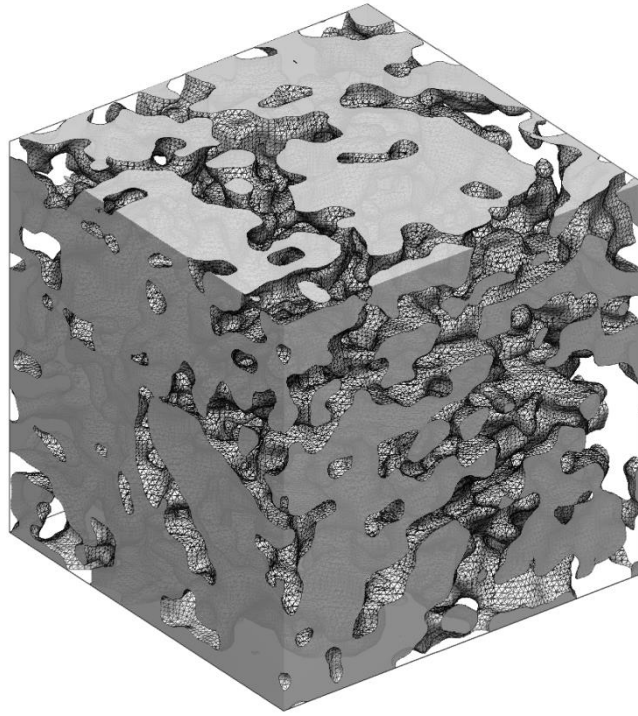


Figure S3. Initial geometry of the simulations shown in Figure 5 (voxel size: 100 nm, GeoID-42136, $\varphi_0 = 0.199$). Fluid flows from the lower left face towards the upper right face.

Table S1. Results of simulations conducted in this study. GeoID is a unique number assigned to each sample used as an initial microstructure in simulations. l indicates the voxel resolution. φ_0 represents the initial porosity of the sample. ChemID is a unique number assigned to each chemical scenario (Table 1). uid is a unique number assigned to each simulation. φ_c indicates the breakthrough porosity. PV_c is the number of pore volumes of fluid to breakthrough. $\delta\varphi_c$ represents the difference between the initial and the breakthrough porosity. “n.a.” indicates a sample dissolves homogeneously.

GeoID	l (nm)	φ_0	ChemID	uid	φ_c	PV_c	$\delta\varphi_c$
9435	25	0.2665	01	97658	n.a.	n.a.	0.7335
9435	25	0.2665	02	29203	0.3994	1.08E+05	0.1329
9435	25	0.2665	03	24461	n.a.	n.a.	0.7335
9435	25	0.2665	04	93567	0.4320	5.00E+04	0.1655
9435	25	0.2665	05	30768	0.4465	5.38E+02	0.1800
9435	25	0.2665	06	84652	0.4707	1.53E+04	0.2042
52235	25	0.2057	01	2736	n.a.	n.a.	0.7943
52235	25	0.2057	02	72086	0.3460	1.21E+05	0.1403
52235	25	0.2057	03	78443	n.a.	n.a.	0.7943
52235	25	0.2057	04	15382	0.3772	5.41E+04	0.1715
52235	25	0.2057	05	53764	0.4529	7.07E+02	0.2472
52235	25	0.2057	06	880	0.4516	1.86E+04	0.2459
53419	25	0.2297	01	63248	0.6931	7.07E+03	0.4634
53419	25	0.2297	02	75810	0.3413	8.79E+04	0.1116
53419	25	0.2297	03	18981	0.6061	9.90E+02	0.3764
53419	25	0.2297	04	67963	0.4006	5.69E+04	0.1709
53419	25	0.2297	05	53091	0.4175	6.23E+02	0.1878
53419	25	0.2297	06	25978	0.4273	1.40E+04	0.1976
60917	25	0.0530	01	42252	0.1878	1.54E+04	0.1348
60917	25	0.0530	02	43265	0.1303	1.20E+05	0.0773
60917	25	0.0530	03	97390	0.0967	2.07E+03	0.0437
60917	25	0.0530	04	35121	0.1829	7.22E+04	0.1299
60917	25	0.0530	05	12273	0.1441	1.11E+03	0.0911
60917	25	0.0530	06	6078	0.2802	3.21E+04	0.2272
82235	25	0.2739	01	25689	n.a.	n.a.	0.7261
82235	25	0.2739	02	65550	0.4053	1.15E+05	0.1314
82235	25	0.2739	03	19540	n.a.	n.a.	0.7261
82235	25	0.2739	04	1879	0.4108	4.09E+04	0.1369
82235	25	0.2739	05	55671	0.4215	4.27E+02	0.1476
82235	25	0.2739	06	62117	0.4684	1.15E+04	0.1945

4888	50	0.2276	01	75994	n.a.	n.a.	0.7724
4888	50	0.2276	02	93376	0.3165	1.00E+05	0.0889
4888	50	0.2276	03	50855	n.a.	n.a.	0.7724
4888	50	0.2276	04	41784	0.3192	3.38E+04	0.0916
4888	50	0.2276	05	73916	0.4243	6.36E+02	0.1967
4888	50	0.2276	06	52242	0.4112	1.24E+04	0.1836
9087	50	0.2118	01	22839	0.2424	1.24E+03	0.0306
9087	50	0.2118	03	90790	0.2800	3.21E+02	0.0682
9087	50	0.2118	04	7930	0.2834	2.54E+04	0.0716
9087	50	0.2118	05	24151	0.5389	8.91E+02	0.3271
9087	50	0.2118	06	22557	0.5496	1.91E+04	0.3378
30168	50	0.2182	01	57121	n.a.	n.a.	0.7818
30168	50	0.2182	02	10976	0.3628	1.72E+05	0.1446
30168	50	0.2182	03	74869	n.a.	n.a.	0.7818
30168	50	0.2182	04	54238	0.3547	4.57E+04	0.1365
30168	50	0.2182	05	57041	0.3982	5.27E+02	0.1800
30168	50	0.2182	06	5281	n.a.	n.a.	0.7818
88470	50	0.1333	01	70913	n.a.	n.a.	0.8667
88470	50	0.1333	02	18747	0.1864	6.76E+04	0.0531
88470	50	0.1333	03	73468	n.a.	n.a.	0.8667
88470	50	0.1333	04	82604	0.2105	3.71E+04	0.0772
88470	50	0.1333	05	79565	0.3733	9.11E+02	0.2400
88470	50	0.1333	06	20898	n.a.	n.a.	0.8667
98562	50	0.1763	01	21682	n.a.	n.a.	0.8237
98562	50	0.1763	02	79784	0.2658	1.24E+05	0.0895
98562	50	0.1763	03	8642	n.a.	n.a.	0.8237
98562	50	0.1763	04	36574	0.2835	4.66E+04	0.1072
98562	50	0.1763	05	97447	n.a.	n.a.	0.8237
98562	50	0.1763	06	91245	0.5506	2.78E+04	0.3743
1832	100	0.2116	01	43103	n.a.	n.a.	0.7884
1832	100	0.2116	02	29158	0.4900	5.75E+05	0.2784
1832	100	0.2116	03	96536	n.a.	n.a.	0.7884
1832	100	0.2116	04	48411	0.3540	5.34E+04	0.1424
1832	100	0.2116	05	82856	0.4370	5.72E+02	0.2254
1832	100	0.2116	06	37819	0.3301	7.73E+03	0.1185
36487	100	0.1899	01	20530	n.a.	n.a.	0.8101
36487	100	0.1899	02	60354	0.2636	8.65E+04	0.0737

36487	100	0.1899	03	29377	n.a.	n.a.	0.8101
36487	100	0.1899	04	45197	0.2957	3.86E+04	0.1058
36487	100	0.1899	05	16956	0.3151	4.13E+02	0.1252
36487	100	0.1899	06	73427	0.2954	7.62E+03	0.1055
42136	100	0.1979	01	3813	n.a.	n.a.	0.8021
42136	100	0.1979	02	96443	0.3936	2.79E+05	0.1957
42136	100	0.1979	03	23133	n.a.	n.a.	0.8021
42136	100	0.1979	04	28767	0.3707	6.15E+04	0.1728
42136	100	0.1979	05	62224	0.4345	5.87E+02	0.2366
42136	100	0.1979	06	16337	0.4215	1.17E+04	0.2236
60234	100	0.1997	01	26582	n.a.	n.a.	0.8003
60234	100	0.1997	02	43249	0.2506	4.31E+04	0.0509
60234	100	0.1997	03	62411	n.a.	n.a.	0.8003
60234	100	0.1997	04	64051	0.3008	3.19E+04	0.1011
60234	100	0.1997	05	24212	n.a.	n.a.	0.8003
60234	100	0.1997	06	94579	0.2281	2.63E+03	0.0284
82949	100	0.1909	01	53545	n.a.	n.a.	0.8091
82949	100	0.1909	02	69476	0.2651	8.04E+04	0.0742
82949	100	0.1909	03	77677	n.a.	n.a.	0.8091
82949	100	0.1909	04	20012	0.3872	7.21E+04	0.1963
82949	100	0.1909	05	46003	0.3501	4.71E+02	0.1592
82949	100	0.1909	06	91577	0.6053	1.73E+04	0.4144
29098	25	0.0331	01	37273	0.2958	1.93E+04	0.2627
29098	25	0.0331	02	67330	0.1214	1.58E+05	0.0883
29098	25	0.0331	03	68680	0.2442	3.19E+03	0.2111
29098	25	0.0331	04	68724	0.1505	7.97E+04	0.1174
29098	25	0.0331	05	49808	0.2148	1.58E+03	0.1817
29098	25	0.0331	06	52768	0.1932	3.42E+04	0.1601
34437	25	0.0538	01	24177	0.1354	1.55E+04	0.0816
34437	25	0.0538	02	42957	0.1346	1.25E+05	0.0808
34437	25	0.0538	03	52245	0.3195	2.32E+03	0.2657
34437	25	0.0538	04	17494	0.2368	9.12E+04	0.1830
34437	25	0.0538	05	70270	0.3776	1.64E+03	0.3238
34437	25	0.0538	06	40030	0.3375	3.38E+04	0.2837
38978	25	0.0117	01	38486	0.0194	1.86E+05	0.0077
38978	25	0.0117	02	45174	0.0890	2.43E+05	0.0773
38978	25	0.0117	03	18980	0.0210	3.24E+04	0.0093

38978	25	0.0117	04	18540	0.1187	1.21E+05	0.1070
38978	25	0.0117	05	33319	0.2294	1.92E+03	0.2177
38978	25	0.0117	06	42172	0.1350	4.89E+04	0.1233
49596	25	0.0620	01	97591	0.1707	1.70E+04	0.1087
49596	25	0.0620	02	60986	0.1473	1.30E+05	0.0853
49596	25	0.0620	03	7369	0.2113	2.65E+03	0.1493
49596	25	0.0620	04	56418	0.2253	9.06E+04	0.1633
49596	25	0.0620	05	52410	0.2040	1.37E+03	0.1420
49596	25	0.0620	06	75510	0.1176	2.04E+04	0.0556
60513	25	0.1035	01	85735	n.a.	n.a.	0.8965
60513	25	0.1035	02	5941	0.2044	1.23E+05	0.1009
60513	25	0.1035	03	48943	n.a.	n.a.	0.8965
60513	25	0.1035	04	44765	0.2353	6.63E+04	0.1318
60513	25	0.1035	05	87848	0.3005	1.26E+03	0.1970
60513	25	0.1035	06	77834	0.2630	2.51E+04	0.1595
49707	100	0.0640	01	84367	n.a.	n.a.	0.9360
49707	100	0.0640	02	48761	0.1365	1.14E+05	0.0725
49707	100	0.0640	03	77226	n.a.	n.a.	0.9360
49707	100	0.0640	04	30262	0.1909	6.76E+04	0.1269
49707	100	0.0640	05	54920	n.a.	n.a.	0.9360
49707	100	0.0640	06	930	0.1051	8.56E+03	0.0411
62954	100	0.0562	01	94868	0.0895	4.75E+03	0.0333
62954	100	0.0562	02	76896	0.0903	6.64E+04	0.0341
62954	100	0.0562	03	26211	n.a.	n.a.	0.9438
62954	100	0.0562	04	64094	0.1936	7.75E+04	0.1374
62954	100	0.0562	05	10574	0.2128	8.69E+02	0.1566
62954	100	0.0562	06	61450	0.0906	8.27E+03	0.0344
63250	100	0.0395	01	16746	n.a.	n.a.	0.9605
63250	100	0.0395	02	39601	0.0640	6.56E+04	0.0245
63250	100	0.0395	03	77205	0.2008	1.39E+03	0.1613
63250	100	0.0395	04	88867	0.1684	7.66E+04	0.1289
63250	100	0.0395	05	98700	n.a.	n.a.	0.9605
63250	100	0.0395	06	47834	0.0771	1.17E+04	0.0376
73318	100	0.0777	01	22017	n.a.	n.a.	0.9223
73318	100	0.0777	02	27294	0.1607	1.33E+05	0.0830
73318	100	0.0777	03	29243	n.a.	n.a.	0.9223
73318	100	0.0777	04	3003	0.1723	5.05E+04	0.0946

73318	100	0.0777	05	20241	0.2197	7.51E+02	0.1420
73318	100	0.0777	06	32205	0.1613	1.12E+04	0.0836
82835	100	0.0541	01	31467	n.a.	n.a.	0.9459
82835	100	0.0541	02	3724	0.1259	1.36E+05	0.0718
82835	100	0.0541	03	37369	0.1735	1.15E+03	0.1194
82835	100	0.0541	04	80241	0.2285	1.22E+05	0.1744
82835	100	0.0541	05	49277	0.1512	8.60E+02	0.0971
82835	100	0.0541	06	50508	0.1407	1.60E+04	0.0866
14228	25	0.0302	01	79728	n.a.	n.a.	0.9698
14228	25	0.0302	02	9236	0.1761	2.04E+05	0.1459
14228	25	0.0302	03	92737	0.2547	3.06E+03	0.2245
14228	25	0.0302	04	80205	0.1767	7.47E+04	0.1465
14228	25	0.0302	05	33626	0.2631	1.44E+03	0.2329
14228	25	0.0302	06	34807	0.2786	3.23E+04	0.2484
20374	25	0.0423	01	85216	0.1522	1.71E+04	0.1099
20374	25	0.0423	02	783	0.2090	2.35E+05	0.1667
20374	25	0.0423	03	44418	0.2538	2.44E+03	0.2115
20374	25	0.0423	04	24344	0.1954	7.98E+04	0.1531
20374	25	0.0423	05	5146	0.3064	1.57E+03	0.2641
20374	25	0.0423	06	68837	0.3000	3.40E+04	0.2577
43457	25	0.0470	01	74069	0.2516	1.75E+04	0.2046
43457	25	0.0470	02	42311	0.1242	1.35E+05	0.0772
43457	25	0.0470	03	52265	0.2050	2.63E+03	0.1580
43457	25	0.0470	04	42654	0.1522	7.89E+04	0.1052
43457	25	0.0470	05	97901	0.2300	1.57E+03	0.1830
43457	25	0.0470	06	68838	0.2097	3.15E+04	0.1627
52989	25	0.1114	01	78241	0.3666	1.25E+04	0.2552
52989	25	0.1114	02	65558	0.2526	1.43E+05	0.1412
52989	25	0.1114	03	52250	0.4042	1.93E+03	0.2928
52989	25	0.1114	04	44637	0.2059	5.25E+04	0.0945
52989	25	0.1114	05	56626	0.3494	1.03E+03	0.2380
52989	25	0.1114	06	32553	0.4901	3.31E+04	0.3787
93330	25	0.0712	01	97509	0.2673	1.61E+04	0.1961
93330	25	0.0712	02	72293	0.1593	1.20E+05	0.0881
93330	25	0.0712	03	89618	0.2865	2.44E+03	0.2153
93330	25	0.0712	04	23495	0.2002	7.19E+04	0.1290
93330	25	0.0712	05	72341	0.2321	1.38E+03	0.1609

93330	25	0.0712	06	96375	0.1661	2.17E+04	0.0949
2891	50	0.0194	01	4686	n.a.	n.a.	0.9806
2891	50	0.0194	02	10882	0.0371	1.13E+05	0.0177
2891	50	0.0194	03	77761	0.1148	4.88E+03	0.0954
2891	50	0.0194	04	51035	0.1741	1.07E+05	0.1547
2891	50	0.0194	05	84515	0.0615	1.46E+03	0.0421
2891	50	0.0194	06	6472	0.0643	2.33E+04	0.0449
27332	50	0.0373	01	18969	n.a.	n.a.	0.9627
27332	50	0.0373	02	53121	0.1288	1.44E+05	0.0915
27332	50	0.0373	03	65882	0.1062	1.88E+03	0.0689
27332	50	0.0373	04	94284	0.1423	6.33E+04	0.1050
27332	50	0.0373	05	36875	0.0835	9.58E+02	0.0462
27332	50	0.0373	06	87058	0.1229	2.20E+04	0.0856
36648	50	0.0555	01	22009	0.0644	1.55E+04	0.0089
36648	50	0.0555	02	63177	0.0804	1.42E+05	0.0249
36648	50	0.0555	03	56841	0.1203	7.48E+03	0.0648
36648	50	0.0555	04	82574	0.0909	1.12E+05	0.0354
36648	50	0.0555	06	76484	0.0758	1.98E+04	0.0203
37398	50	0.0524	01	4215	n.a.	n.a.	0.9476
37398	50	0.0524	02	12650	n.a.	n.a.	0.9476
37398	50	0.0524	03	50598	0.0548	2.01E+03	0.0024
37398	50	0.0524	04	74129	0.0926	1.17E+05	0.0402
37398	50	0.0524	05	1956	0.0841	1.31E+03	0.0317
37398	50	0.0524	06	28046	0.1079	1.95E+04	0.0555
81804	50	0.0327	01	16092	0.1294	1.89E+04	0.0967
81804	50	0.0327	02	13431	n.a.	n.a.	0.9673
81804	50	0.0327	03	67782	0.1338	2.62E+03	0.1011
81804	50	0.0327	04	13124	0.0964	8.09E+04	0.0637
81804	50	0.0327	05	61746	0.0506	1.58E+03	0.0179
81804	50	0.0327	06	47310	0.0545	2.75E+04	0.0218
2913	100	0.0549	01	39251	0.2534	7.30E+03	0.1985
2913	100	0.0549	03	39807	0.2621	1.11E+03	0.2072
2913	100	0.0549	04	56532	0.2054	8.91E+04	0.1505
2913	100	0.0549	05	72804	n.a.	n.a.	0.9451
2913	100	0.0549	06	39595	n.a.	n.a.	0.9451
50569	100	0.0482	01	57899	0.1812	9.10E+03	0.1330
50569	100	0.0482	02	77273	0.1500	2.12E+05	0.1018

50569	100	0.0482	03	35846	0.1871	1.36E+03	0.1389
50569	100	0.0482	04	72475	0.1414	6.15E+04	0.0932
50569	100	0.0482	05	52010	0.1669	9.59E+02	0.1187
50569	100	0.0482	06	60085	0.0917	1.15E+04	0.0435
74505	100	0.0393	01	74396	n.a.	n.a.	0.9607
74505	100	0.0393	02	69644	0.1002	1.14E+05	0.0609
74505	100	0.0393	03	79614	n.a.	n.a.	0.9607
74505	100	0.0393	04	83242	0.1229	5.37E+04	0.0836
74505	100	0.0393	05	81467	0.2571	1.09E+03	0.2178
74505	100	0.0393	06	62583	0.1532	1.86E+04	0.1139
78782	100	0.0511	01	65698	0.1730	7.66E+03	0.1219
78782	100	0.0511	02	12534	0.1120	1.02E+05	0.0609
78782	100	0.0511	03	6525	0.2225	1.17E+03	0.1714
78782	100	0.0511	04	45156	0.1503	5.59E+04	0.0992
78782	100	0.0511	05	26325	0.1778	8.72E+02	0.1267
78782	100	0.0511	06	51883	0.1955	1.84E+04	0.1444
91338	100	0.0602	01	62676	n.a.	n.a.	0.9398
91338	100	0.0602	02	13016	0.1190	1.24E+05	0.0588
91338	100	0.0602	03	62727	0.1121	9.81E+02	0.0519
91338	100	0.0602	04	97899	0.1433	5.86E+04	0.0831
91338	100	0.0602	05	48393	0.1808	9.40E+02	0.1206
91338	100	0.0602	06	6759	0.0828	7.24E+03	0.0226

REFERENCES

1. Plummer, L. N.; Busenberg, E., The solubilities of calcite, aragonite and vaterite in CO₂-H₂O solutions between 0 and 90 C, and an evaluation of the aqueous model for the system CaCO₃-CO₂-H₂O. *Geochimica et Cosmochimica Acta* **1982**, *46*, (6), 1011-1040.
2. Pokrovsky, O. S.; Golubev, S. V.; Schott, J.; Castillo, A., Calcite, dolomite and magnesite dissolution kinetics in aqueous solutions at acid to circumneutral pH, 25 to 150 C and 1 to 55 atm pCO₂: new constraints on CO₂ sequestration in sedimentary basins. *Chemical geology* **2009**, *265*, (1), 20-32.
3. Pokrovsky, O. S.; Golubev, S. V.; Schott, J., Dissolution kinetics of calcite, dolomite and magnesite at 25 C and 0 to 50 atm pCO₂. *Chemical Geology* **2005**, *217*, (3), 239-255.
4. Subhas, A. V.; Rollins, N. E.; Berelson, W. M.; Dong, S.; Erez, J.; Adkins, J. F., A novel determination of calcite dissolution kinetics in seawater. *Geochimica et Cosmochimica Acta* **2015**, *170*, 51-68.